

Research Article

Permeability and Microstructure of a Saline Intact Loess after Dry-Wet Cycles

Jian Xu ^{1,2}, Chang Ren ¹, Songhe Wang ³, Jingyu Gao ¹ and Xiangang Zhou ³

¹School of Civil Engineering, Xi'an University of Architecture and Technology, Xi'an, Shaanxi 710055, China

²Shaanxi Key Laboratory of Geotechnical and Underground Space Engineering, Xi'an University of Architecture and Technology, Xi'an, Shaanxi 710055, China

³State Key Laboratory of Eco-Hydraulics in Northwest Arid Region, Xi'an University of Technology, Xi'an, Shaanxi 710048, China

Correspondence should be addressed to Jian Xu; xujian@xauat.edu.cn and Songhe Wang; wangsonghe@xaut.edu.cn

Received 22 October 2020; Revised 22 February 2021; Accepted 28 February 2021; Published 11 March 2021

Academic Editor: Gang Zhou

Copyright © 2021 Jian Xu et al. This is an open access article distributed under the Creative Commons Attribution License, which permits unrestricted use, distribution, and reproduction in any medium, provided the original work is properly cited.

Influenced by both dry-wet cycles and salt weathering, the loess will exhibit significant changes in microstructure and permeability, which threatens the stability of loess slopes. Triaxial permeability tests and industrial computed tomography (CT) scans were carried out on saline intact loess with sodium sulfate. The relationship between permeability and pore structure of the loess after dry-wet cycles was discussed. Results show that the permeability coefficient of loess increases after dry-wet cycles, with the increment declining. After specified dry-wet cycles, the permeability coefficient increases approximately linearly with sodium sulfate content. However, the permeability coefficient significantly declines at higher confining pressures, while its attenuation rate decreases. An empirical relationship based on $\log_{10}(1 + e) - \log_{10}(k)$ was proposed to estimate the permeability coefficient of saline intact loess considering dry-wet cycles and salt content. Comparisons of measured and calculated results proved its rationality. CT scan images imply the damage to soil microstructure induced by dry-wet cycles and salt weathering, corresponding to the decline of the mean CT value (ME) and the increase of both crack ratio and fractal dimension of crack network.

1. Introduction

The loess in Northwest China inevitably experiences dry-wet cycles due to the arid and semiarid climatic conditions. The structure of the loess is seriously changed after long-term wetting-drying cycles, resulting in varying permeability and deformation characteristics [1]. In addition, the loess is affected by salt weathering effect, which causes structural change inside the loess mass, e.g., reordering the arrangement of soil particles [2, 3]. Salt weathering is characterized by three processes. The first is the migration of solutes in the soil under dry-wet actions, synchronously with that of water, which leads to agglomeration of the soluble salts in a local area. The second is the crystallization of migrated soluble salts under the surface evaporation, with soil structure loosened, and consequently the permeability coefficient significantly increases. The third is the repeated process of crystallization-dissolution of solutes, mainly the sodium

sulfate (Na_2SO_4) as revealed by field surveys, that causes the structural change of the eroded soil to expand and thus the internal cracks gradually develop [4]. Salt weathering is a frequently encountered phenomenon in the loess region, developed in the loess in different stratigraphic ages, paleosol and compacted loess. Induced by both dry-wet cycles and salt weathering, the natural environment of the loess region, which is already very fragile, is easy to form a gradual stripping of surface soils of the slope and even leads to landslides [4, 5].

Studies have shown that the extension of cracks in the soil and the permeability is closely related to the dry-wet cycles [6–8]. More obvious changes in soil structure and permeability may occur when soluble salts are involved [9]. Albrecht and Benson [10] investigated the shrinkage of natural clay after dry-wet cycles, with cracks generated during drying and the permeability coefficient increased by three orders. Malusis et al. [11] found that the permeability

coefficient of the soil increased with dry-wet cycles and significant changes occurred in the case of higher vertical deformation. Wan et al. [12] noticed different responses of the permeability of compacted clay in low and high degrees of compaction to dry-wet cycles in view of the microstructure. Shen et al. [13] noticed that salt weathering induced damage to saline soil in earthen archaeological site in Northwest China. Wen et al. [14] noticed the influence of hysteresis behavior after dry-wet cycles on the permeability of the soil. Rayhani et al. [15] carried out a study on the permeability of fractured clay and found that with the increase of plasticity index and clay content, the fracture size and permeability coefficient of soil samples increased after dry-wet cycles. A further study by Rayhani et al. [16] proved that cracking of the large-sized sample would lead to an increase in permeability coefficient, sometimes up to 5–10 orders of magnitude and the permeability coefficient of high-plasticity soil decreased after longer permeation due to self-healing. Lu et al. [17] noticed that the pore volume of the loess in landfills grew after dry-wet cycles while the pore size showed little change, and the permeability coefficient increased positively with pore volume and more pronounced cracks. Wan et al. [18] analyzed the influence of the liquid limit of compacted clay cushion (CCL) on its structure and permeability after dry-wet cycles, and both the crack ratio and the permeability coefficient grew at higher liquid limit. From the previous work, the relationship between soil permeability and microstructure has been investigated by tests. However, the coupled influence of dry-wet cycling and salt weathering on the permeability coefficient of saline intact loess was rarely reported in recent literature studies.

Under the dual action of dry-wet and salt weathering, the cracks on the loess surface develop to varying degrees, which was considered as an important cause of natural hazards such as ground fissures, ground subsidence, collapse, and landslides [19]. At present, many scholars have studied the microstructure of rock and soil mass by different experimental methods, such as mercury intrusion porosimetry and scanning electron microscope [20–22]. Tang et al. [23] proposed a method of quantifying microscopic images of soil pores and particles based on image processing technology, which can be effectively applied in investigating the soil particle morphology and pore structure evolution. The CT scan, as a common nondestructive testing method, is widely used in microstructure research [24, 25]. Kawaragi et al. [26] carried out permeability test and CT scan test on bentonite to explore the relationship between the permeability and microstructure and results showed that the difference of microstructure was closely related to the permeability, dependent on its degree of saturation. Julina and Thyagaraj [27] investigated the influence of salinity on the fracture morphology of compacted clay during dry-wet cycles by using CT technology and the results show that the permeability coefficient considerably grows due to the salt-induced crack extension. Luo et al. [28] observed the dynamic transport of solute in the soil column based on CT technology. Li et al. [29] used the CT technology to scan the Malan loess with macroscopic pore characteristics of the Malan loess characterized by quantitative parameters. Peth

et al. [30] quantitatively compared pore structures of the two types of soils in conventionally tilled and grassland. Qiu et al. [31] used micro-CT scanning technology to scan coal samples, reconstructed the micropore model, and simulated the seepage behaviors of gas and water. However, the evolution of the microstructure of saline intact loess induced by dry-wet cycling and salt weathering has rarely been discussed.

Under dry-wet cycling, saline intact loess with sodium sulfate (Na_2SO_4) is affected by both the volume change (i.e., shrinkage during drying and swelling when wetting) and salt weathering (i.e., the volume of crystalline sodium sulfate increased to 4.18 times and consequently induced the deterioration of soil structure). In this study, the sodium sulfate solution (Na_2SO_4) with mass fractions of 0.0%, 0.5%, 1.0%, and 1.5% was infiltrated into the intact loess by means of a self-designed saline infiltration method to prepare undisturbed saline loess samples with different salinities. The coupled effects of dry-wet and salt weathering on the permeability and microstructure of saline intact loess were investigated by using the triaxial permeability test and CT scan test. The relationship between permeability and microstructure of saline intact loess after dry-wet cycles was discussed.

2. Materials and Methods

2.1. Soil Specimen Preparation. The loess samples were taken from a foundation pit in Xi'an, China, with sampling depth of 6–8 m, which can be classified as Q_3 loess. The physical properties of the loess were determined based on the standard for soil test method (GB/T 50123-2019) while the ion types and contents were measured by ion chromatography and titration, as listed in Table 1. The extremely low mass fractions for the considered ions indicate that the influence of the original soluble salts can be neglected in preparing saline intact loess specimens.

In order to reveal the salt weathering effect of intact loess, it is necessary to prepare the saline intact loess specimens with preset Na_2SO_4 contents, which can hardly be satisfied by on-site sampling due to its large dispersion. Thus, a self-designed infiltration method was adopted here. The specific procedure for preparing saline intact loess specimens at preset Na_2SO_4 contents is as follows. Cylindrical soil specimens for triaxial tests and CT scans were cut from soil blocks, with diameter of 3.91 cm and height of 8.0 cm. Following the procedure for preparing saline intact loess specimens [4], i.e., the self-designed saline infiltration method, the gravimetric water content w was controlled to be 20% and four Na_2SO_4 contents η were considered, i.e., 0.0%, 0.5%, 1.0%, and 1.5%. The method uses a sponge filled with a certain proportion of saline water to wrap a soil sample with a perforated film.

Then, after infiltrating for a period when the Na_2SO_4 solution evenly penetrated the intact loess, the prepared saline loess specimen was taken out and weighed. When the weight was close to the target value, the solution was slowly added to the soil specimen by a dropper so that the continual immersion of the solution exceeding the target value can be avoided. The prepared soil specimens wrapped with plastic

TABLE 1: Initial properties of the tested loess.

Property	Value	Initial ion contents (%)	Value
Specific gravity, G_s	2.70	Anions	
Initial dry density, ρ_{d0} (g/cm^3)	1.49	CO_3^{2-}	0.0016
Atterberg limits		HCO_3^-	0.0333
Plastic limit, w_p (%)	19.00	Cl^-	0.0006
Liquid limit, w_L (%)	36.50	SO_4^{2-}	0.0056
Particle grading characteristics (%)		Cation	
>0.05 mm	2.95	K^+	0.0016
0.01–0.05 mm	54.42	Ca^{2+}	0.0061
0.005–0.01 mm	20.55	Na^+	0.0032
<0.005 mm	22.08	Mg^{2+}	0.0034

film were placed in a moisturizing tank for 24 h, so that the solution can be evenly distributed. In order to reduce the test error, it is necessary to repeat the test and strictly control the infiltration time to ensure the accuracy of the test result. The trial tests on the uniformity of salt and water contents in soil specimen [4] prove that this method can produce saline intact loess specimens at a target salt content and minimize the disturbance to soil structure during solution infiltration.

Before triaxial permeability test, the soil was initially saturated by the vacuum saturation method. The soil specimen after dry-wet cycles ($N=0, 1, 2, 5, \text{ and } 10$) was placed into the three-valve saturator, which was then put into a cylindrical saturation tank for vacuum pumping for 1 h. During pumping, the vacuum pressure gauge was kept constant. Distilled water was injected into the saturation tank until the water level overflows the saturator. The vacuum pumping was stopped and the intake valve of the saturation cylinder was turned on to ensure that the pressure inside the saturation cylinder slowly rises to atmospheric pressure so that the distilled water can slowly infiltrate into the soil to minimize the disturbance to soil structure. The soil specimen was immersed in the water for 12 h.

2.2. Test Plan

2.2.1. Dry-Wet Tests. For each dry-wet cycle during tests, two stages of drying and wetting are included. During drying process, in order to more accurately control the ambient temperature and drying time, an electrothermostatic blast oven with effective temperature range of 10–300°C and maximum temperature fluctuation of $\pm 1.0^\circ\text{C}$ was used. An ambient temperature of 40°C was preset in the blast oven to be as close as possible to the natural environment (i.e., the maximum atmospheric temperature in summer). Trial tests were carried out to determine the drying time required for the soil at a water content of 20.0% to be dried to a constant value lower than 1.0%. Firstly, four groups of standard soil specimens for triaxial tests were cut from soil blocks, with a diameter of 3.91 cm and a height of 8.0 cm. Secondly, soil specimens at four target salt contents were prepared by the saline infiltration method. After removing the wrapped layers such as sponge and perforated film, saline soil specimens were placed into the electrothermostatic blast oven with an ambient temperature of 40°C. Finally, the water content of the soil was measured after drying for five target durations, i.e., 6, 12, 18,

24, and 30 h. Figure 1 presents the variation of water content of the soil at each considered salt content. It shows that the water content of the soil decreases to less than 1.0% after drying for 24 h, which can be taken as the drying time at an ambient temperature of 40°C. During wetting, the dried soil was wrapped with the perforated film and the sponge with distilled water to reach a target water content of 20.0%. Then the perforated film and the sponge were removed and the soil wrapped by a new preservative film was placed into a chamber with constant temperature and humidity for 24 h. This is called a dry-wet cycle. In this study, the dry-wet cycles were controlled to be 0, 1, 2, 5, and 10.

2.2.2. Triaxial Permeability Tests. A varying-head triaxial permeameter [32] was used in triaxial permeability tests. Five main steps were included in the triaxial permeability test, as shown below.

Step I. After vacuum saturation in accordance with the standard for soil test methods (GB/T 50123-2019), the soil specimen was taken out of the three-valve saturator and wrapped with a latex film. It was then put into a pressure chamber for triaxial permeability test, with both ends of the latex film tightly fixed by rubber rings to the top plate and the base. After the tempered glass cover is covered, the fixing nut between the base and the tempered glass cover was tightened.

Step II. Distilled water was injected into the pressure chamber through the valve for confining pressure. When there is water overflow in the exhaust plug at the upper end of the pressure chamber, the exhaust plug was immediately tightened and the water injection was stopped. The inlet pipe, the outlet pipe, and the confining pressure tube were, respectively, connected with the varying head pipe, water collection bottle, and the valve for confining pressure. The inlet valve of the pressure chamber was closed. Then, distilled water was added to the varying head pipe to the scale of 100 cm, and the confining pressure valve and the outlet valve were opened, with the confining pressure adjusted to be the same as the water head pressure. The inlet valve was opened to allow water to flow through the inside of the soil. When there are no bubbles flowing out of the water outlet and the inflow and outflow are the same, it means that the soil has reached saturation.

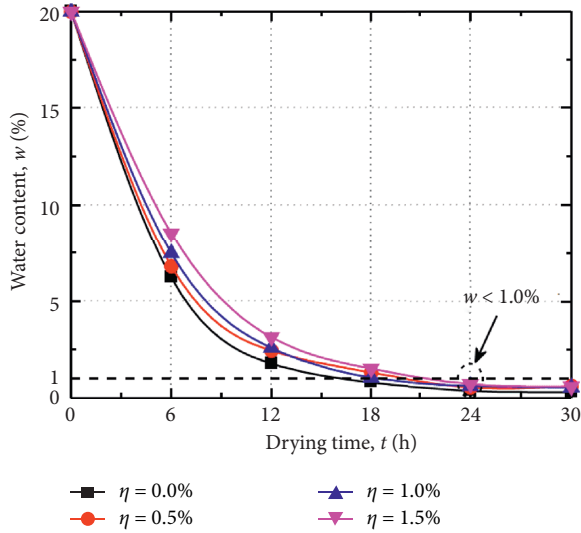


FIGURE 1: Variation of water content of the tested soil over drying time.

Step III. Both the inlet valve and the outlet valve of the pressure chamber were closed, and the confining pressure was adjusted to 15 kPa with the liquid level in the airless tube read. The outlet valve of the pressure chamber was opened. When the liquid level in the airless tube no longer dropped and no water was discharged through the outlet, the soil was considered to be completely consolidated. The stable liquid level in the airless tube was recorded.

Step IV. Distilled water was added to the varying head pipe to the scale of 100 cm again and the inlet valve was opened to allow distilled water to flow through the soil. When water flows out of the outlet, the initial water head height in the varying head tube and the start time were recorded. After a certain duration, the inlet valve was closed with the water head height in the varying head tube and the end time recorded, and the temperature of water at the outlet was measured by a thermometer. Based on the above data, the permeability coefficient of the soil is converted by the equation of the varying head permeability coefficient. Repeat the above steps 5 to 6 times, and take the average value as the permeability coefficient of the soil under the current confining pressure.

Step V. The confining pressure adjustment knob was slowly turned to reach a target confining pressure (i.e., 50, 100, and 150 kPa). After the soil is fully consolidated, the permeability coefficient was measured according to the above steps.

The permeability coefficient of the soil k can be calculated by

$$k = 2.3 \frac{aL}{A_{cs}(t_2 - t_1)} \log \frac{H_1}{H_2}, \quad (1)$$

where a is the cross-sectional area of the varying head pipe (cm^2); L is the seepage path, i.e., the height of the intact loess

(cm); A_{cs} is the cross-sectional area of the soil (cm^2); t_1 and t_2 are the start and stop time of water head measurement (s); and H_1 and H_2 are the water heads corresponding to t_1 and t_2 (cm).

The permeability coefficient of the soil at a standard temperature of 20°C can be calculated by

$$k_{20} = k_T \frac{\eta_T}{\eta_{20}}, \quad (2)$$

where k_{20} is the permeability coefficient of soil at $T = 20^\circ\text{C}$ (cm/s); η_T is the kinematic viscosity coefficient at a temperature of T (kPa·s); and η_{20} is the kinematic viscosity coefficient at $T = 20^\circ\text{C}$ (kPa·s). Based on the standard for soil test method (GB/T 50123-2019), the viscosity ratio η_T/η_{20} is illustrated in Figure 2. From the monitored temperatures of water at the outlet, as illustrated in the top right corner, a range of $19.9\text{--}25.2^\circ\text{C}$ was noted, with the mean value of 22.6°C , which corresponds to a viscosity ratio of 0.94.

2.2.3. Industrial CT Scan Tests. Four soil specimens with different salt contents ($\eta = 0.0\%$, 0.5% , 1.0% , and 1.5%) after specified dry-wet cycles ($N = 0, 1, 2, 5,$ and 10) were scanned to analyze the effect of dry-wet cycles and salt content on soil microstructure, respectively. Herein, the dried soils after preset dry-wet cycles were tested by means of the industrial CT scan apparatus, i.e., the YXLON Y.CT Modula. The maximum diameter for a measured cross section is 100 mm, and the maximum height for the measured specimen is 200 mm. The maximum magnification and maximum spatial resolution are 200 times and $10 \mu\text{m}$. The saline intact loess specimen after preset dry-wet cycles was marked with a directional arrow and placed in the above industrial CT machine for microscopic scanning. Each time, the saline intact loess specimen was scanned from the X -axis, the Y -axis, and the Z -axis in three directions. The microstructure image of the specimen can be obtained by scanning, and the mean CT value (ME) can be further determined through image processing. Herein, the ME value reflects the average density of all material points in the scanning section. The lower the soil density, the lower the ME, so the change in ME can reflect the internal damage of the soil. In addition, the Particles (Pores) and Cracks Analysis System (PCAS) [33–35] was also used to quantify the CT scan image (the density map of a section) of saline intact loess.

3. Results and Analysis

3.1. Permeability Coefficient of Saline Intact Loess. Figure 3 shows the effect of dry-wet cycles on the permeability coefficient of saline intact loess. Four levels of confining pressure were plotted, i.e., 15, 50, 100, and 150 kPa. Under a given confining pressure, the permeability coefficient of soil at a certain salt content increases positively with dry-wet cycles. However, the increment of the permeability coefficient with respect to dry-wet cycle experiences obvious decline. Before the fifth cycle, the permeability coefficient increases rapidly, while it exhibits a significantly lowering growth rate after five cycles and consequently tends to reach

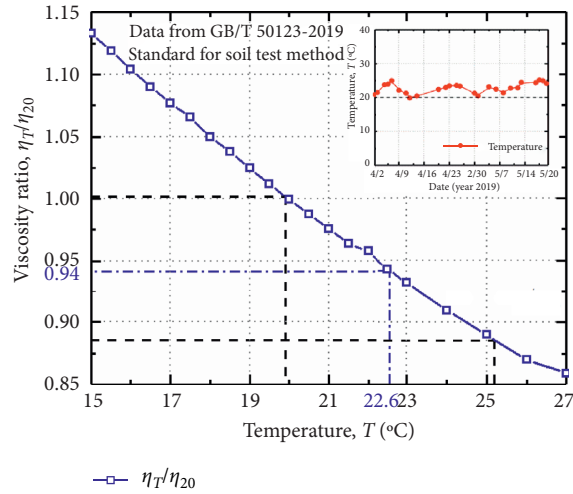


FIGURE 2: Viscosity ratio for pure water at various temperatures (based on the standard for soil test method GB/T 50123-2019).

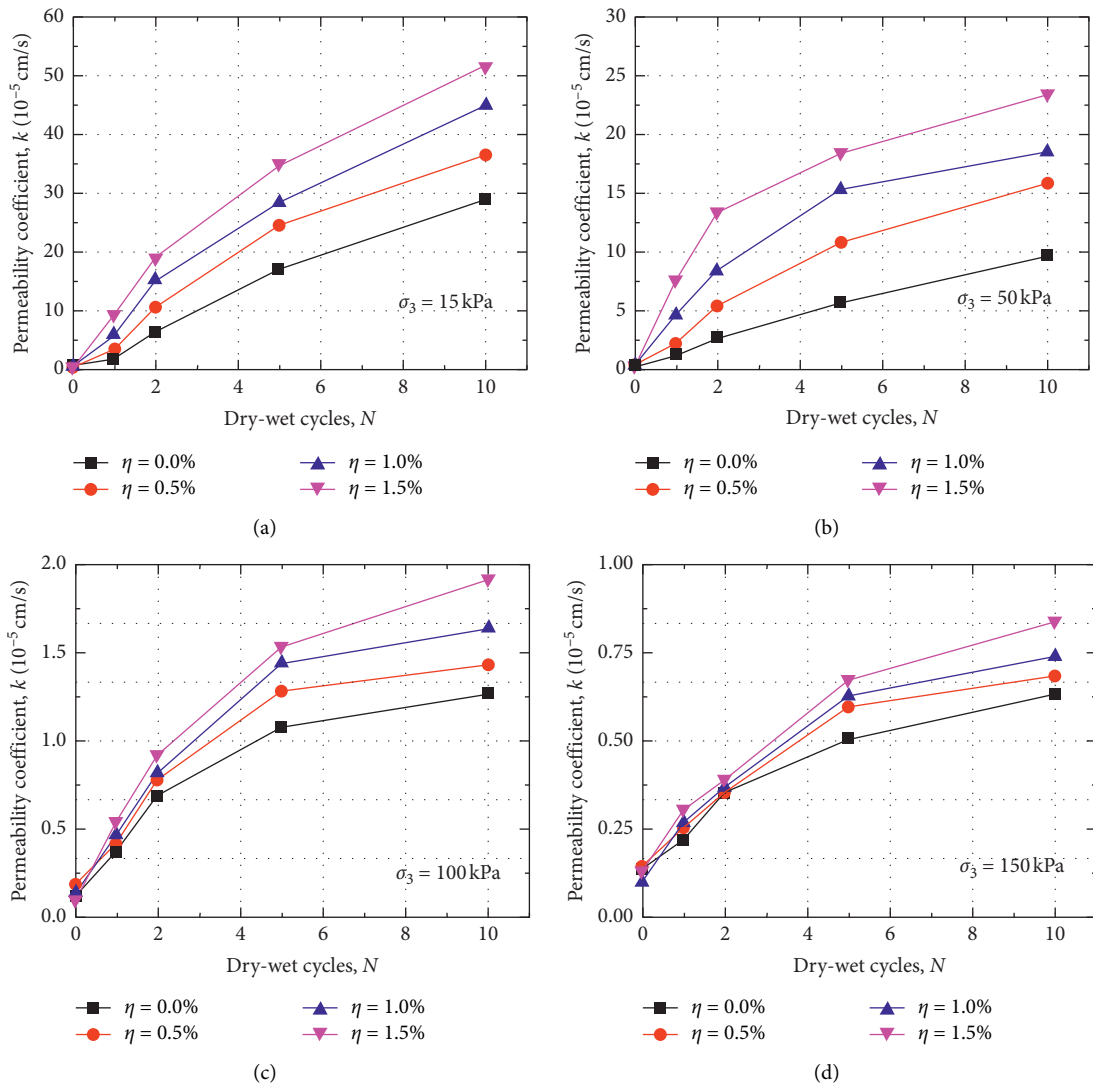


FIGURE 3: Permeability coefficient of saline intact loss after dry-wet cycles. (a) $\sigma_3 = 15$ kPa, (b) $\sigma_3 = 50$ kPa, (c) $\sigma_3 = 100$ kPa, and (d) $\sigma_3 = 150$ kPa.

a stable value. Regarding the effect of dry-wet cycles, the schematic diagram given in Figure 4(a) can be combined for the analysis. Influenced by temperature and water, the soil specimen shrinks during drying and swells when wetting. Soil pores and microcracks in the soil continue to expand after dry-wet cycles, implying the potential irreversible damage to the structure. This further leads to the weakening of soil structure and lower strength of the loess as a macroscopic response, which provides a good seepage channel for water. The permeability coefficient increases accordingly. After multiple dry-wet cycles, soil structure tends to be stable with a stable residual strength of the soil, and the permeability coefficient also approaches a constant value.

Figure 5 shows the variation of the permeability coefficient with salt content. It can be seen from the figure that the permeability coefficient increases approximately linearly with sodium sulfate content after dry-wet cycles. From the schematic shown in Figure 4(b), the influence of salt content on the permeability can be interpreted by the repeated salt weathering due to the crystallization-dissolution-recrystallization process of the sodium sulfate in the soil during dry-wet cycles. A very noteworthy phenomenon in this process is that after sodium sulfate (Na_2SO_4) crystallizes into sodium sulfate decahydrate ($\text{Na}_2\text{SO}_4 \cdot 10\text{H}_2\text{O}$), its volume increases to 4.18 times. Therefore, the soil structure becomes looser; that is, the opening of pores or microcracks in the soil becomes larger, which leads to an increase in the permeability coefficient. It is worth noting that the permeability coefficient at $N=0$ does not change significantly with salt content, mainly since no phase change of sodium sulfate occurs before dry-wet cycles. Thus, the permeability coefficient shows little change in this case.

The permeability coefficients of saline intact loess at considered confining pressures are shown in Figure 6. It shows that the permeability coefficient decreases at higher confining pressures. At $\sigma_3 = 150$ kPa, the permeability coefficient approaches a constant value. From Figure 4(c), the soil will be compressed at higher the confining pressures, with more pores or cracks compressed or even closed, which will block the seepage channels. The permeability coefficient declines as a result. Besides, as the confining pressure exceeds 100 kPa, the permeability coefficients of soil specimens after dry-wet cycles show limited changes, indicating the insignificant effect of dry-wet cycles. This is also related to the higher degree of consolidation at higher confining pressures.

3.2. Permeability Model for Saline Intact Loess after Dry-Wet Cycles. The typical permeability models that describe the relationship between permeability coefficient k and void ratio e are summarized in Table 2. Compared to the other models, the empirical equation proposed by Liu et al. [41] well estimates the permeability coefficient of naturally deposited clay, which required only one parameter. Considering that the saline intact loess exhibits a certain bonding effect between soil particles, thus we employed this equation to reflect the relationship between permeability coefficient and void ratio. Herein, the relationship between void ratio, dry-wet cycles, and salt content during triaxial permeability

test is plotted in Figures 7 and 8. The results show that the void ratio of the soil at various confining pressure increases with dry-wet cycles with lower increment and exhibits an approximately linear variation with salt content after dry-wet cycles. This well corresponds to the changes of permeability coefficient with dry-wet cycle and salt content, which also reveals the changes of permeability coefficient. In addition, it is worth noting that the void ratio at $N=0$ varies insignificantly with salt content (Figure 8), which probably results from the fact that the phase change of sodium sulfate in loess rarely occurs before dry-wet cycles.

Considering the effect of void ratio, dry-wet cycle, and salt content on the permeability coefficient of saline intact loess, an empirical relationship was proposed, as shown below:

$$\bar{e} = A\bar{k} + B, \quad (3)$$

with

$$\bar{e} = \log_{10} \left(\frac{1+e}{1+e_0} \right), \quad (4)$$

$$\bar{k} = \log_{10} \left(\frac{k_0}{k} \right),$$

where k_0 is the initial permeability coefficient and A and B are fitted parameters related to soil property. From Figure 9, the data fitting results prove that the coefficients of regression are higher than 0.80 under the considered test conditions. For soil at $N=0$ and $\sigma_3 = 15$ kPa, the sodium sulfate solution in soil pores is maintained at a stable state without phase change. Thus, the porosity for this soil can be taken as the initial value of e_0 , corresponding to the initial permeability coefficient k_0 , i.e., $e_0 = 0.825$ and $k_0 = 6.05 \times 10^{-6}$ cm/s.

The fitted parameter A after various dry-wet cycles is shown in Figure 10(a). For the sake of simplicity, a linear relationship between the parameter A and dry-wet cycles N can be obtained:

$$A - A_0 = m\bar{N}, \quad (5)$$

with

$$\bar{N} = \frac{N}{N+1}, \quad (6)$$

where A_0 is the initial value of parameter A , equal to -0.04724 , and m is the fitted parameter. From Figure 10(b), the parameter B shows little change with dry-wet cycles, ranging from 0 to -0.025 , and thus, the mean value of B can be taken, i.e., $B = -0.01734$.

From Figure 11, the relationship between m and η was further fitted as

$$m = p\eta + q, \quad (7)$$

where η is the salt content and p and q are fitted parameters.

Thus, the relationship between permeability coefficient and void ratio incorporating dry-wet cycles and salt content was shown below:

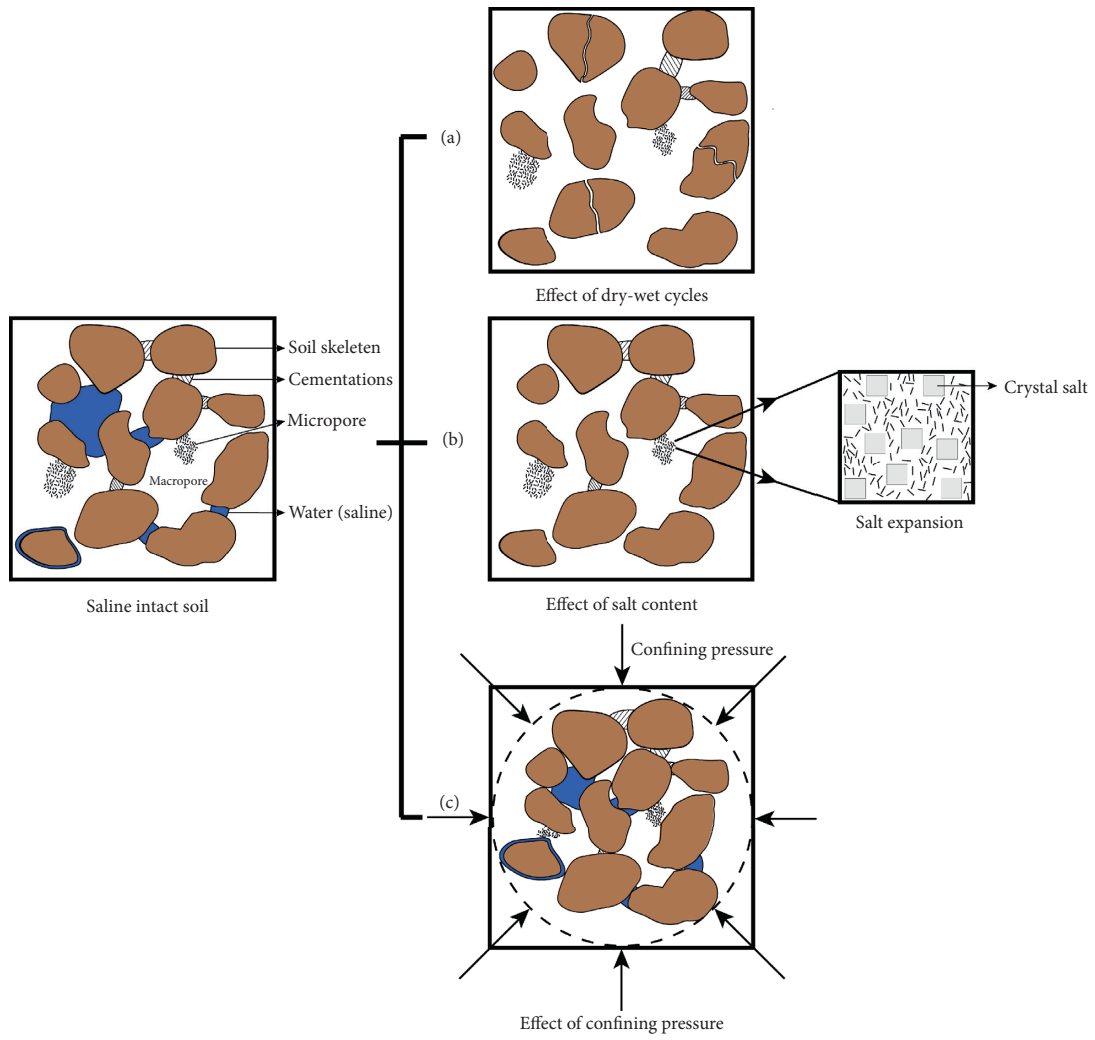


FIGURE 4: Schematic diagram for the influence of dry-wet, salt content, and confining pressure on soil structure.

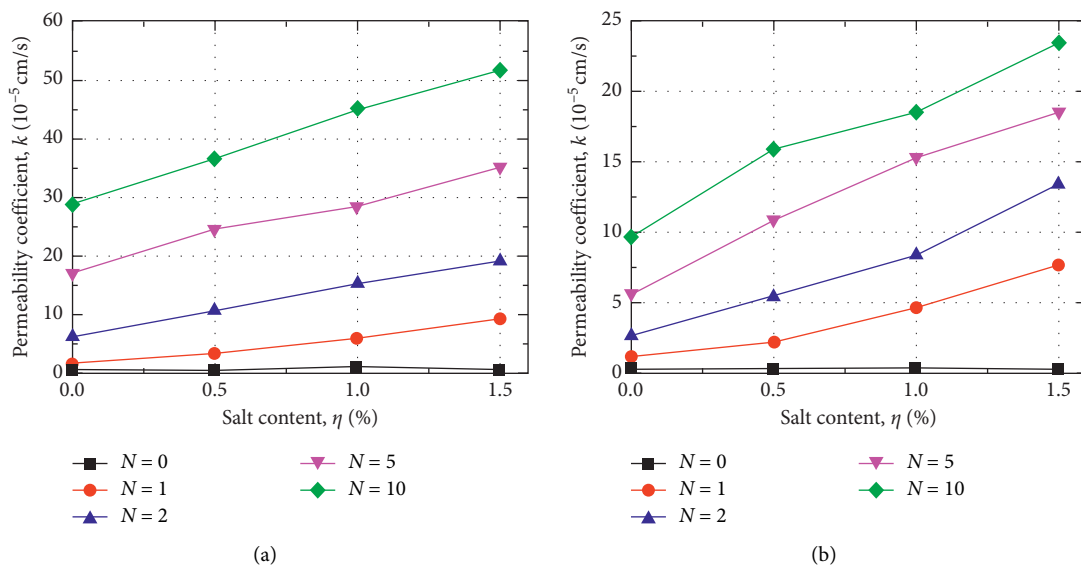


FIGURE 5: Continued.

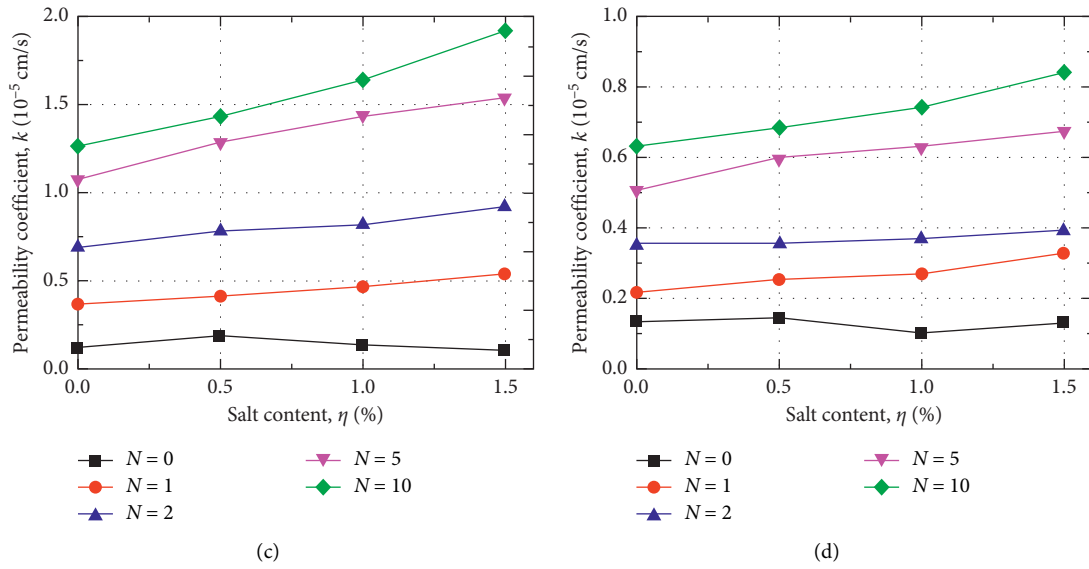


FIGURE 5: Permeability coefficient of saline intact loess at various salt contents. (a) $\sigma_3 = 15$ kPa, (b) $\sigma_3 = 50$ kPa, (c) $\sigma_3 = 100$ kPa, and (d) $\sigma_3 = 150$ kPa.

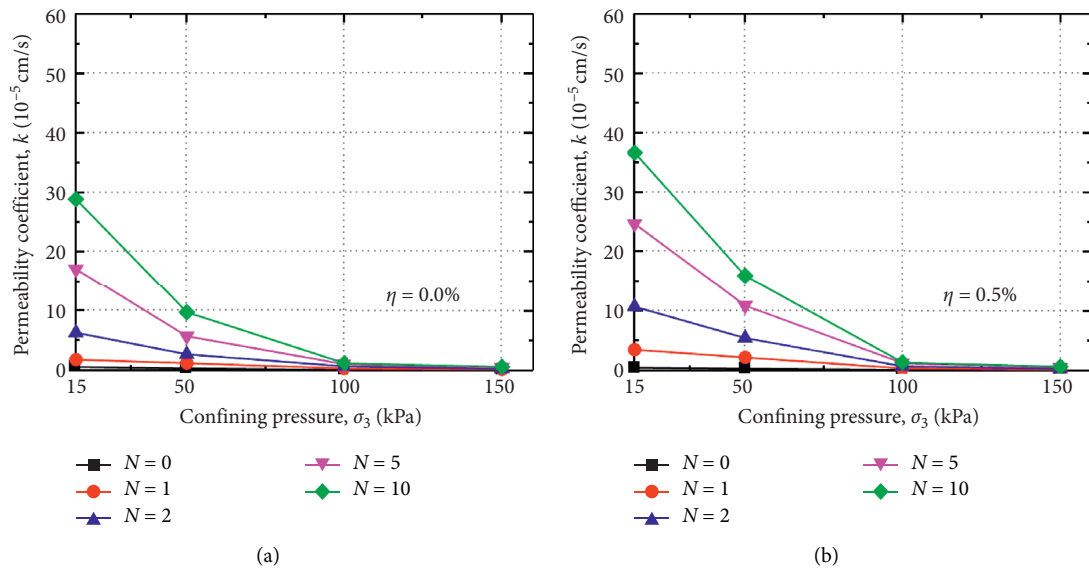


FIGURE 6: Continued.

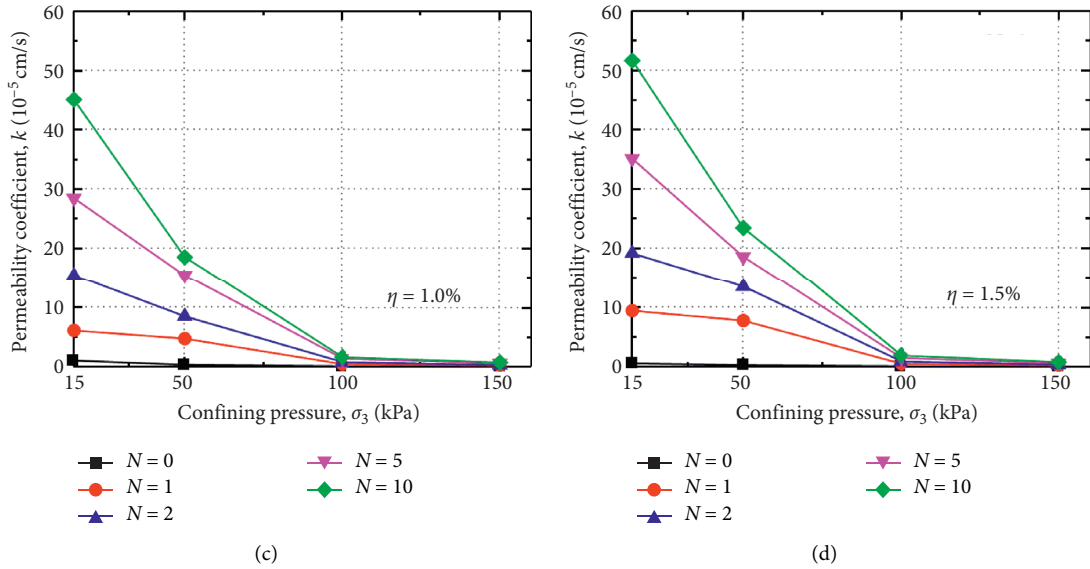


FIGURE 6: Permeability coefficient of saline intact loess at various confining pressures. (a) $\eta = 0.0\%$, (b) $\eta = 0.5\%$, (c) $\eta = 1.0\%$, and (d) $\eta = 1.5\%$.

TABLE 2: Typical permeability models.

No.	Equations	References	Parameters	Applicable condition
1	$k = 2.4622 (d_{10}^2 (e^3/1 + e))^{0.7825}$	[36]	d_{10} : effective diameter C_p^* : material constant	Silty sand
2	$k_p = C_p^* (G_s^{2x-2} / \gamma_w \mu_w) (e^{3+x} / (1 + e) e_L^{2x})$	[37]	G_s : specific gravity of solid particles μ_w : dynamic viscosity e_L : void ratio corresponding to the liquid limit w_l in saturated state	Plastic soil and clay soil
3	$e - e_0 = C_k \log(k/k_0)$	[38]	k_0 : hydraulic conductivity for a reference void ratio e_0 ; C_k : permeability change index	Soft clay
4	$\log k = A_k \log e + B_k$	[39]	A_k, B_k : parameters reflecting permeability characteristics of soil	Large strain
5	$\log[k(1 + e)] = \log C + n \log e$	[40]	C: a constant with the same unit as k ; n : a constant that depends on soil type	Normally consolidated clay
6	$\log(1 + e/1 + e_0) = C'_k \log(k/k_0)$	[41]	C'_k : permeability index	Natural saturated clay

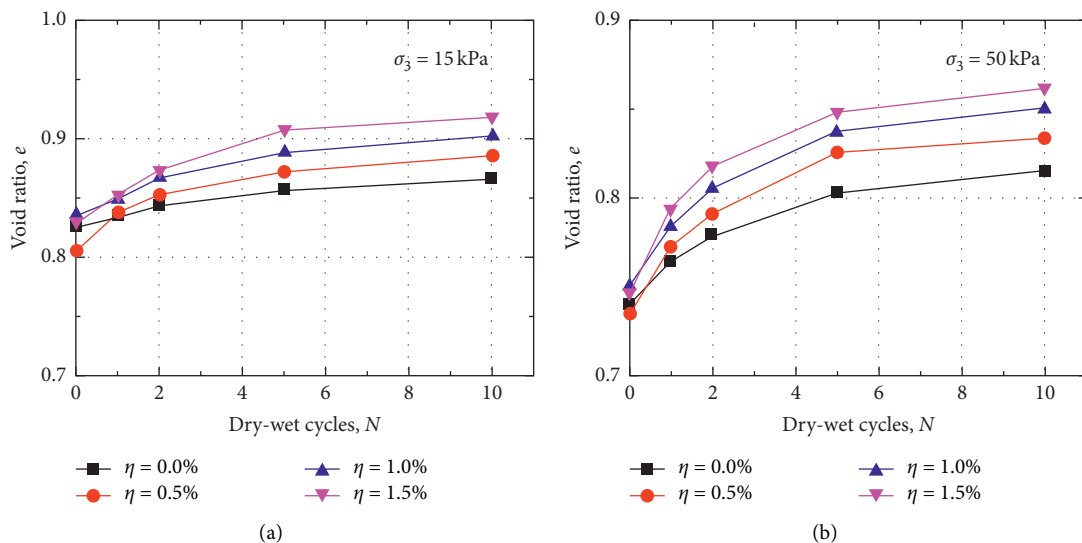


FIGURE 7: Continued.

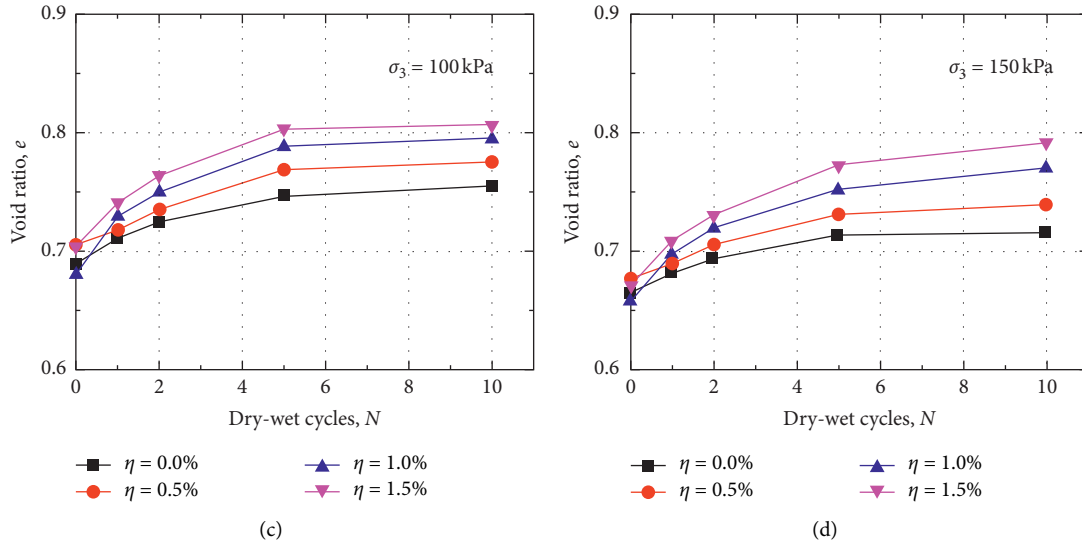


FIGURE 7: The void ratio of saline intact loess after dry-wet cycles.

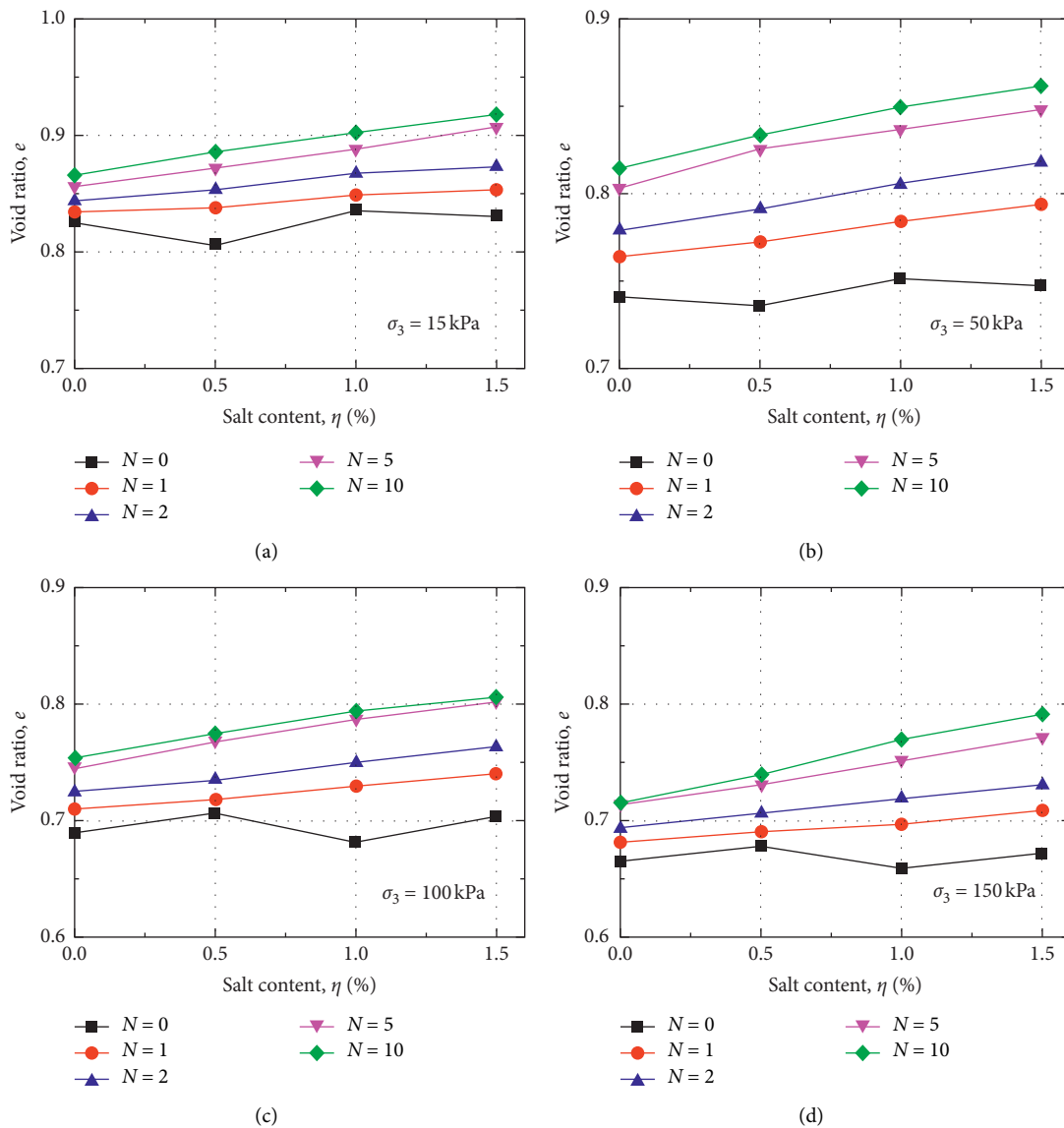


FIGURE 8: The void ratio of saline intact loess at various salt contents.

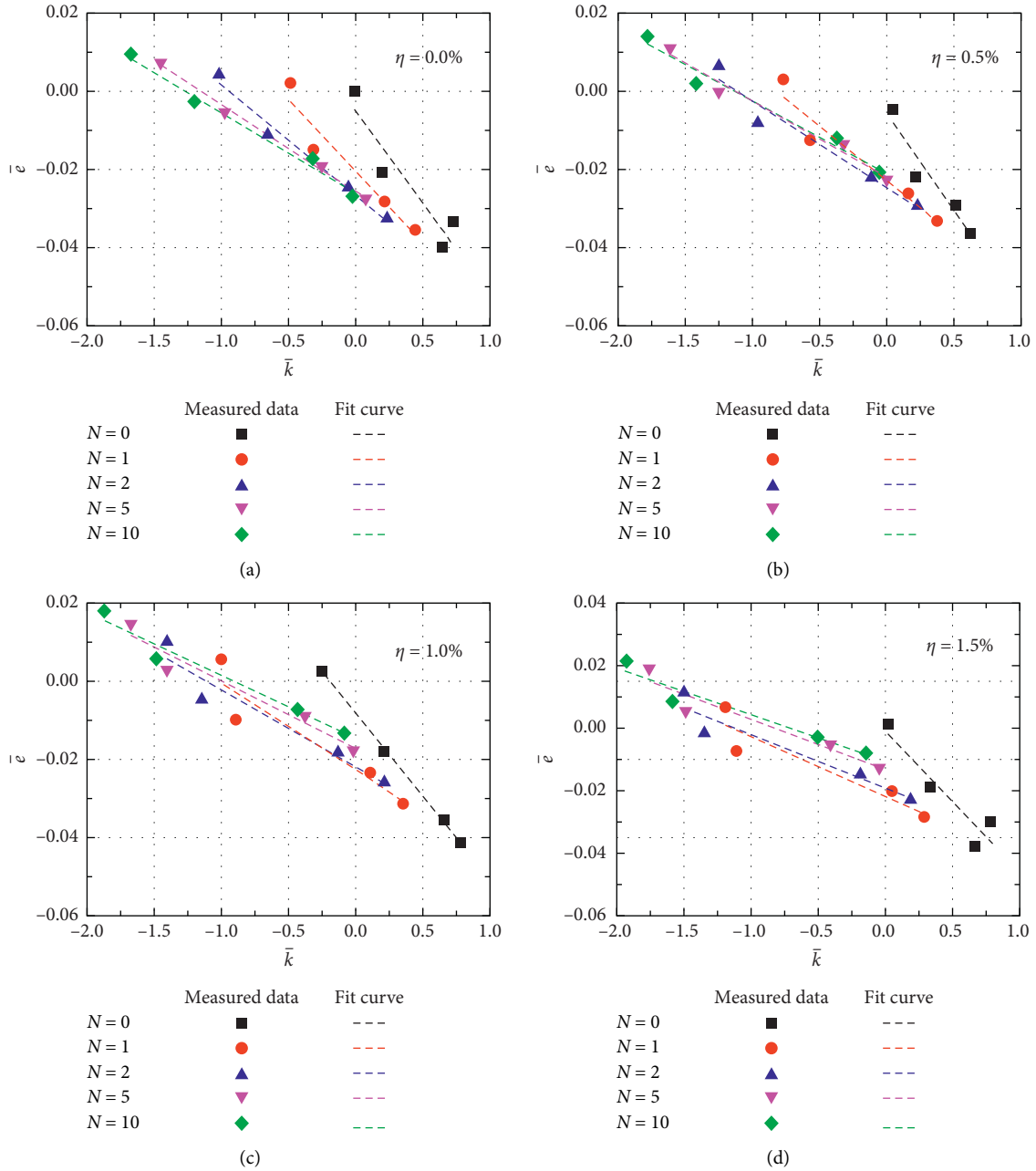


FIGURE 9: Relationship between \bar{k} and \bar{e} .

$$\bar{e} = [(p\eta + q)\bar{N} + A_0]\bar{k} + B. \quad (8)$$

The parameters can be obtained based on data fitting, i.e., $k_0 = 6.05 \times 10^{-6}$ cm/s, $e_0 = 0.825$, $A_0 = -0.04724$, $B = -0.01734$, $p = 0.00794$, and $q = 0.0296$. Comparisons of calculated and measured data, as shown in Figure 12(a), prove that the data points are evenly distributed around the straight line of $y = x$. Figure 12(b) shows the box diagram for fitting errors, i.e., the deviation between calculated and measured data. The upper and lower quartiles are spaced between 25% and 75%. The two ends of the box diagram are the maximum and minimum errors, respectively. The white rectangular box in the middle represents the mean error, with the white horizontal line as

the median value of the error. It proves that the mean value of the error varies between -0.2 and 0.2 , and the median value varies between -0.3 and 0 , indicating a good fitting effect. The deviation between the measured and fitted data is relatively higher at $\sigma_3 = 15$ kPa, compared to higher confining pressures, which may be associated with the lower degree of consolidation. This equation considers the effect of dry-wet cycle and salt content on the permeability coefficient of saline intact loess. Only the number of dry-wet cycles and salt content are required to be determined for the above relationship. This also provides a novel idea to estimate the permeability coefficient under the action of dry-wet cycles in saline loess regions.

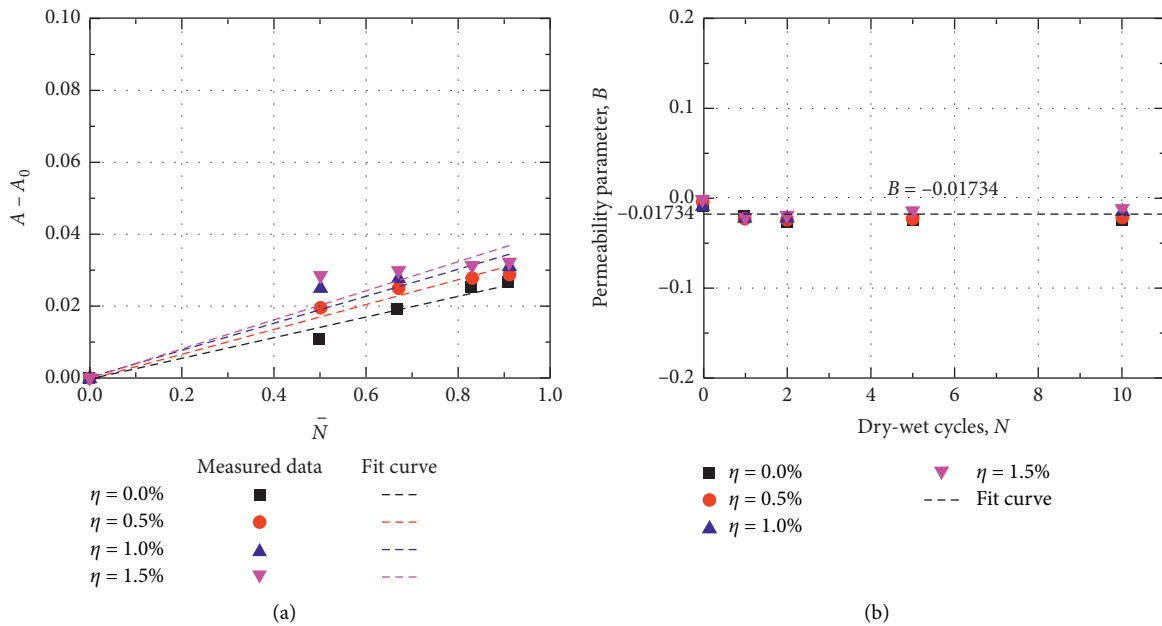


FIGURE 10: Fit results for parameters A and B. (a) Parameter A. (b) Parameter B.

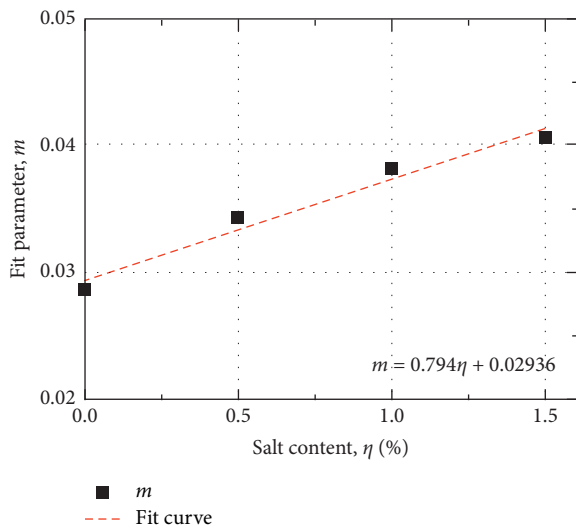


FIGURE 11: Fit result for parameter m .

3.3. Analysis of CT Scan Results

3.3.1. Effect of Dry-Wet Cycles and Salt Content on Soil Microstructure. The CT images of saline intact loess after dry-wet cycles are presented in Figure 13. The grayscale of CT images is in general proportion to the density of the material in a considered domain. The darker the grayscale, the smaller the density. The gray domain represents the material at higher densities while the black area is where the holes and cracks exist. The change to soil structure, from the CT images, manifests in three main forms of damage induced by the expansion of holes, increase of length and width of microcracks, and consequently penetration of holes and microcracks. The initially scanned image shows that

some holes and microcracks exist in the cross section, indicating a certain damage effect in the initial state of undisturbed loess. As dry-wet cycling proceeds, the extension of cracks generally starts with smaller cracks in the original structure. The cracks increase and widen from smaller cracks to those at larger sizes and the holes inside the soil also gradually expand. Under dry-wet cycles, the undisturbed loess samples are affected by temperature and water, which leads to the formation and expansion of dry-shrinkage cracks in the samples. Accordingly, the original microcracks extend, and new cracks are generated. Synchronously, the originally independent holes gradually penetrate each other. When the soil is soaked with water again, the independent holes that penetrated after drying are also filled with free water. When the free water migrates inside the soil, the cracks further increase. At the beginning of the dry-wet cycle, the primary cracks first expand and further connect with adjacent cracks, manifesting as widening of original cracks and generation of new cracks.

The CT scan images of saline intact loess at the four considered salt contents are illustrated in Figure 14. As shown in Figure 14(a), even before dry-wet cycle ($N=0$), some holes and microcracks are not evenly distributed in the scanned sections of the soil, while the CT scan images exhibit no obvious variation with salt content. This behavior is due to phase change of sodium sulfate rarely occurring before dry-wet cycle, which will cause no damage to soil structure that the CT images reflect. However, by comparing the CT scan images at $N=5$ (Figure 14(b)), it can be noticed that the development of cracks varies with salt content. For soils at higher salt contents, the range of expansion for holes increases, and the cracks expand and widen to some extent. Simultaneously, the new holes and cracks appear, and consequently more pronounced changes of soil morphology

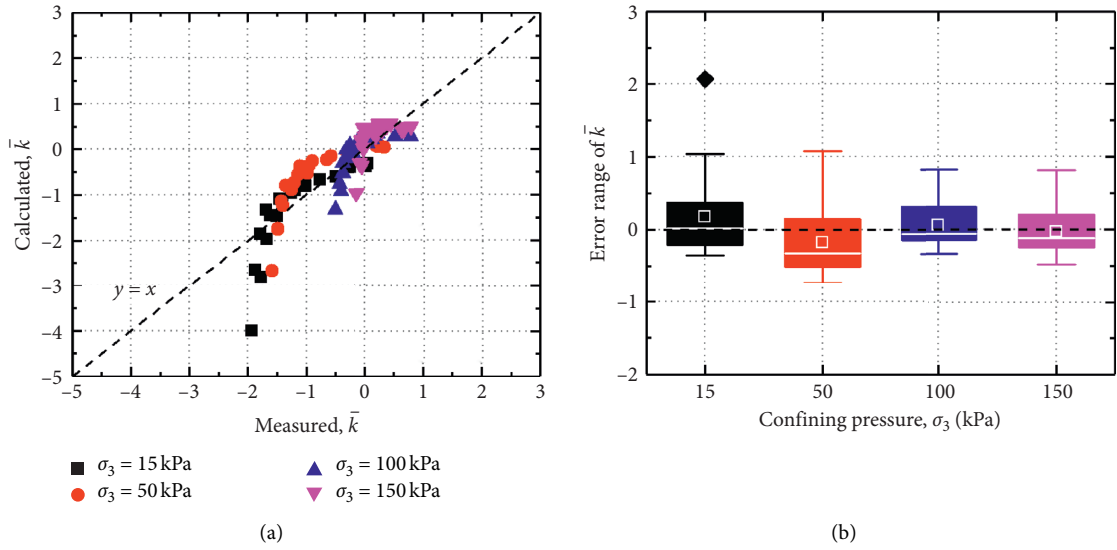


FIGURE 12: Fitting results. (a) Comparison of calculated and measured results. (b) Box diagram for fitting error.

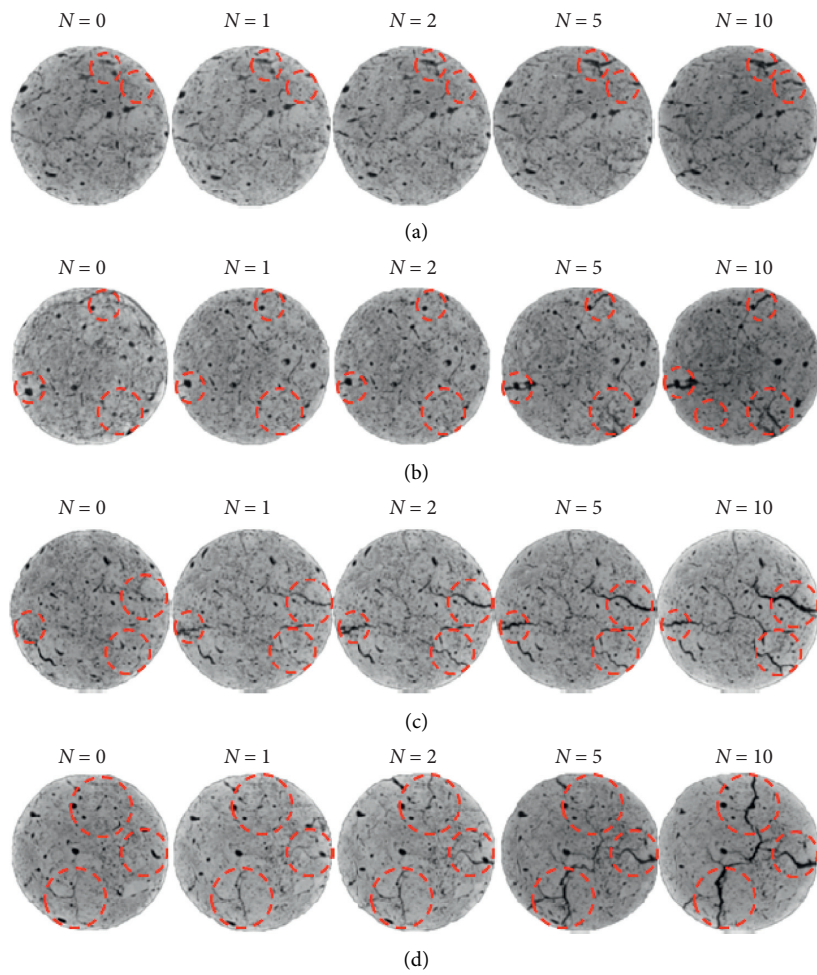


FIGURE 13: CT scan images of saline intact loess after dry-wet cycles. (a) $\eta = 0.0\%$, (b) $\eta = 0.5\%$, (c) $\eta = 1.0\%$, and (d) $\eta = 1.5\%$.

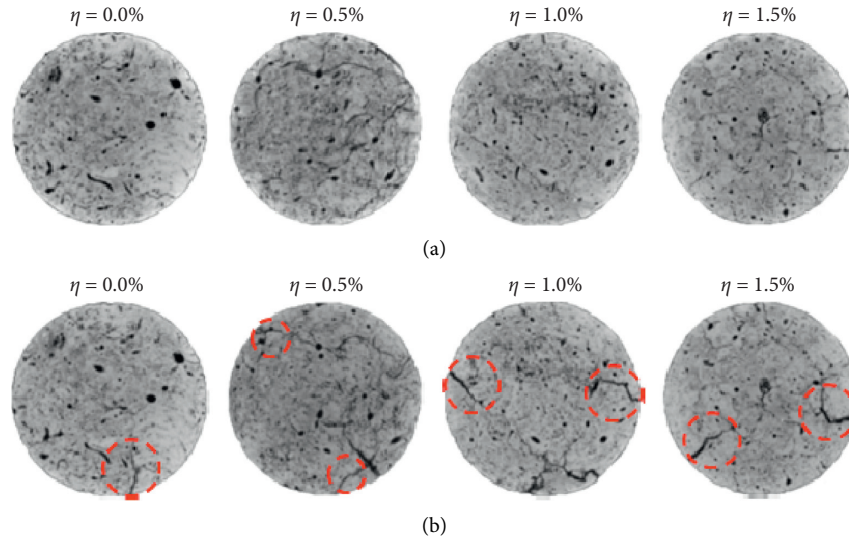


FIGURE 14: CT scan images of saline intact loess at various salt contents. (a) $N=0$. (b) $N=5$.

occur in the scanned sections compared to nonsaline soils, especially for soils at a salt content of 1.5%. At the initial state before dry-wet cycle, sodium sulfate in saline loess mainly exists in the form of unsaturated solution, while, during drying, as a result of water evaporation, the concentration of sodium sulfate solution in the soil specimens grows. Accordingly, the crystal precipitation of sodium sulfate solution occurs in the form of $\text{Na}_2\text{SO}_4 \cdot 10\text{H}_2\text{O}$, with the volume expanded by 3.18 times that of anhydrous sodium sulfate. Therefore, soil voids are significantly expanded with the bonding between soil particles destroyed, and both the length and the width of microcracks grow.

3.3.2. Effect of Dry-Wet Cycles and Salt Content on the CT Value. The ME data of the saline intact loess after dry-wet cycles are shown in Figure 15(a). The ME value of the saline intact loess attenuates obviously with dry-wet cycles. During the initial dry-wet cycles, the ME value of the soil shows a higher attenuation rate. As the dry-wet cycles continue to increase, the rate of attenuation for the ME value declines. The above changes reflect higher rates of damage to soil microstructure at the initial stage of the dry-wet cycles; that is, the internal microcracks of the soil grow faster under initial dry-wet cycles, while the damage effect is weakened after multiple dry-wet cycles. This well reveals the relationship between permeability coefficient and void ratio with dry-wet cycles (Figures 3 and 7).

Figure 15(b) presents the variations of ME value with salt content. Under the dry-wet cycling conditions, the ME value shows an approximately linear attenuation at higher salt contents. The above changes imply that the development of microstructure damage rate of the soil after dry-wet cycles tends to be stable with the increase of salt content. The internal microcracks of the soil continue to expand, and the salt weathering effect is gradually enhanced. This also explains the variation of permeability coefficient and void ratio with salt content in the permeability test (Figures 5 and 8). It

is worth noting that the ME value of the loess before dry-wet cycles ($N=0$) does not change significantly with salt content, which results from the fact that no phase change of sodium sulfate occurs before dry-wet cycles.

3.3.3. Analysis of Crack Morphology of Saline Intact Loess. The morphology of crack network of the saline intact loess during dry-wet condition can be accurately quantified by the PCAS, and the detailed procedure for quantifying soil cracks by means of the PCAS system is shown in Figure 16. Four main steps were included, i.e., obtaining the square image representing the cross section of the test specimen (Step I), binary processing the image by the PCAS system (Step II), skeletonization of the binary image with black line as the cracks in the considered domain (Step III), and identification of surface cracks (Step IV).

Herein, two characteristic indexes can be applied in further analysis including the crack ratio and fractal dimension. The crack ratio, λ_c , represents the ratio of the crack area A_{cr} to the total area A_t , i.e.,

$$\lambda_c = \frac{A_{cr}}{A_t}. \quad (9)$$

The fractal dimension of cracks, D_f , defines the complexity of the crack network of saline intact loess, which can be written as

$$\log C = \frac{D_f}{2} \log S + C_1, \quad (10)$$

where C and S are the perimeter and area of the cracks and C_1 is a fitted parameter.

The loess in general has higher content of silt, vertical joint, and macroporous structure, and crack network is generated inside the soil under the action of dry-wet circulation. As shown in Figure 17(a), the crack ratio increases with dry-wet cycles, and after the second cycle, the increment declines. At the initial five cycles, the growth of crack

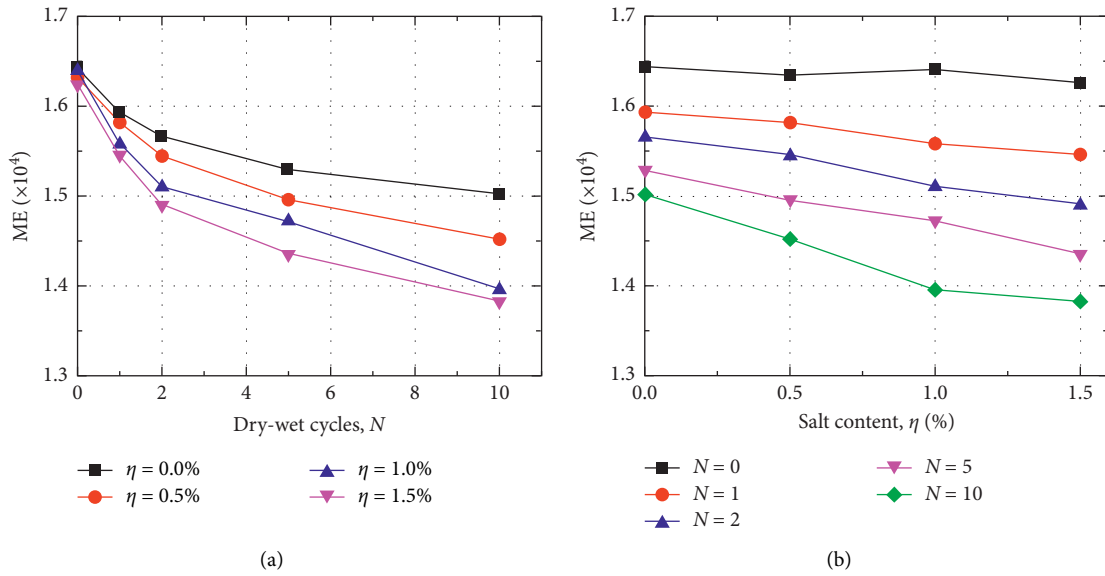


FIGURE 15: Variations of ME. (a) Effect of dry-wet cycles. (b) Effect of salt content.

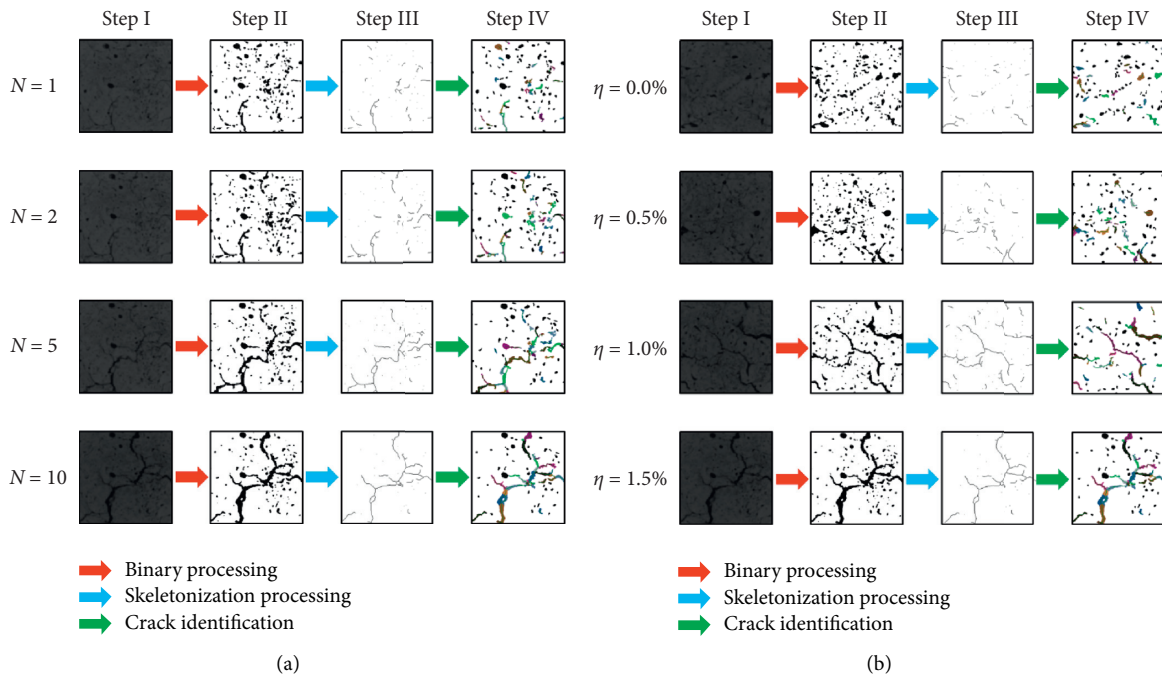


FIGURE 16: Identification of cracks in the soil. (a) After dry-wet cycles. (b) At various salt contents.

ratio accounts for the major proportion, which indicates that the damage caused by dry-wet cycles is mainly concentrated in the first five cycles. Moreover, the fractal dimension of cracks exhibits the similar variation with crack ratio, which is primarily affected by the width and length of microcracks. Figure 17(b) presents the variation of quantified indexes of crack network for soils with respect to salt content at $N = 10$. At the four considered salt contents, the number and width of cracks gradually increase, and the crack ratio increases

approximately linearly with salt content. Besides, the fractal dimension of cracks also experiences a similar increase with respect to salt content.

Figure 18 illustrates the correlations of quantified indexes of cracks with the previous porosity and permeability coefficient of soil specimen for permeability test during dry-wet condition ($\sigma_3 = 15$ kPa and $\eta = 1.5\%$). The crack ratio λ_c reflects the damage information of cross section of soil specimen, and the distribution of microcracks can be well

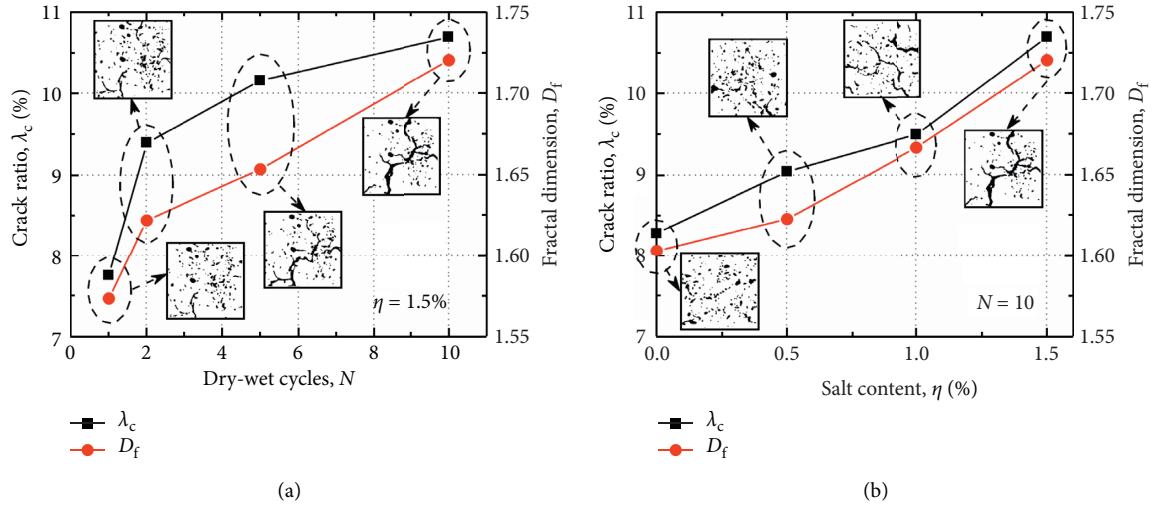


FIGURE 17: Quantified indexes for crack network. (a) Effect of dry-wet cycles. (b) Effect of salt content.

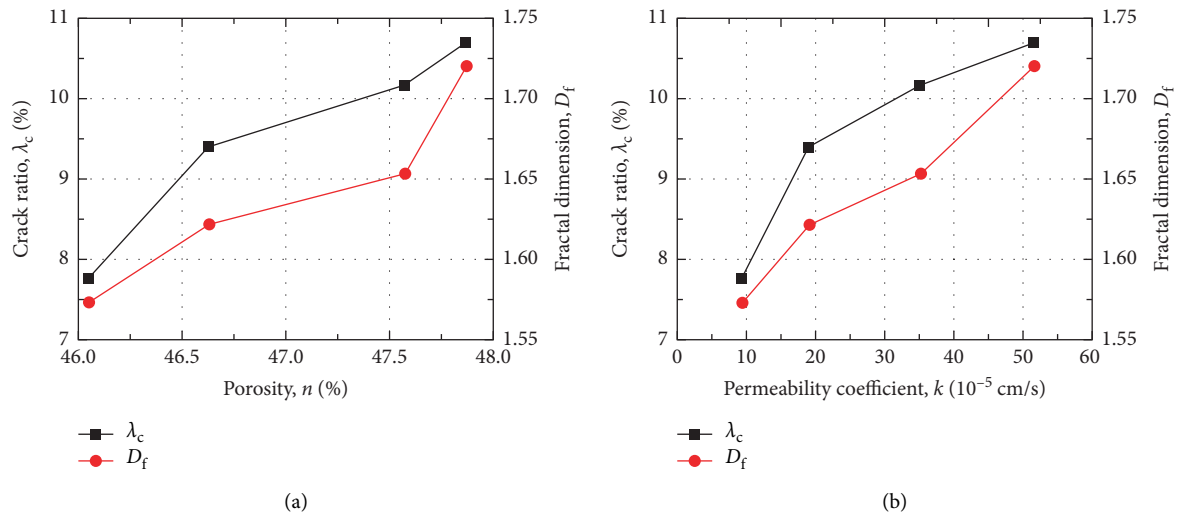


FIGURE 18: Correlations of quantified indexes of cracks with porosity and permeability coefficient. (a) Variation with porosity. (b) Variation with permeability coefficient.

quantified by crack ratio, while the porosity reflects the overall void in the soil. Therefore, the crack ratio and the porosity are positively correlated. The fractal dimension D_f characterizes the complexity of the cracks, which is related to the perimeter and area of the cracks. The higher the fractal dimension, the more complex the spatial distribution of the crack is, or the stronger the capacity of the crack (void) to occupy the space of the soil, the more serious the damage to soil structure will be. It can be further deduced that the permeability coefficient of the soil will be consequently enhanced as seepage paths in the soil are more developed, mainly manifesting as higher crack ratio and more complex crack network.

4. Conclusions

In this study, the permeability of saline intact loess after dry-wet cycles and its correlation with microstructure were investigated based on triaxial permeability tests and

industrial computed tomography (CT) scans. The main conclusions are as follows:

- (1) The permeability coefficient of saline intact loess increases positively under more dry-wet cycles or at higher salt contents while decreases at higher confining pressures. Based on the $\log_{10}(1+e) - \log_{10}(k)$ relationship, an empirical model was proposed considering both dry-wet cycles and salt content, which could well estimate the permeability coefficient of saline intact loess after dry-wet cycles.
- (2) The variations of the permeability coefficient of saline intact loess well correspond to the changes of ME with respect to dry-wet cycle and salt content. Quantified indexes of crack morphology in CT scan images, i.e., the crack ratio and fractal dimension, further prove that cracks inside the loess are more developed after dry-wet cycles or at higher salt

contents, thus providing more developed seepage paths for pore solution.

Data Availability

The data used to support the findings of this study are available from the corresponding author upon request.

Conflicts of Interest

The authors declare that there are no conflicts of interest regarding the publication of this article.

Acknowledgments

The research described in this paper was financially supported by the National Natural Science Foundation of China (nos. 51878551, 51478385, and 51778528), the Research Fund of the State Key Laboratory of Eco-hydraulics in Northwest Arid Region, Xi'an University of Technology (Grant no. 2019KJCXTD-12), and the China Scholarship Council (CSC). These supports are greatly appreciated.

References

- [1] J. Wang, T. Gu, M. Zhang, Y. Xu, and J. Kong, "Experimental study of loess disintegration characteristics," *Earth Surface Processes and Landforms*, vol. 44, no. 6, pp. 1317–1329, 2019.
- [2] S. H. Wang, Q. Z. Wang, J. L. Qi, and F. Y. Liu, "Experimental study on freezing point of saline soft clay after freeze-thaw cycling," *Geomechanics and Engineering*, vol. 15, no. 4, pp. 997–1004, 2018.
- [3] Q. Z. Wang, J. L. Qi, S. H. Wang, J. Xu, and Y. G. Yang, "Effect of freeze-thaw on freezing point of a saline loess," *Cold Regions Science and Technology*, vol. 170, Article ID 102922, 2020.
- [4] J. Xu, Y. Li, S. Wang, Q. Wang, and J. Ding, "Shear strength and mesoscopic character of undisturbed loess with sodium sulfate after dry-wet cycling," *Bulletin of Engineering Geology and the Environment*, vol. 79, no. 3, pp. 1523–1541, 2019.
- [5] J. Xu, Y. Li, C. Ren, and W. Lan, "Damage of saline intact loess after dry-wet and its interpretation based on SEM and NMR," *Soils and Foundations*, vol. 60, no. 4, pp. 911–928, 2020.
- [6] K. Hall and A. Hall, "Weathering by wetting and drying: some experimental results," *Earth Surface Processes and Landforms*, vol. 21, no. 4, pp. 365–376, 1996.
- [7] V. Y. Chertkov, "Using surface crack spacing to predict crack network geometry in swelling soils," *Soil Science Society of America Journal*, vol. 64, no. 6, pp. 1918–1921, 2000.
- [8] I. A. Sadisun, H. Shimada, M. Ichinose, and K. Matsui, "Study on the physical disintegration characteristics of Subang claystone subjected to a modified slaking index test," *Geotechnical and Geological Engineering*, vol. 23, no. 3, pp. 199–218, 2005.
- [9] D. Liu, D. She, and X. Mu, "Water flow and salt transport in bare saline-sodic soils subjected to evaporation and intermittent irrigation with saline/distilled water," *Land Degradation & Development*, vol. 30, no. 10, pp. 1204–1218, 2019.
- [10] B. A. Albrecht and C. H. Benson, "Effect of desiccation on compacted natural clays," *Journal of Geotechnical and Geoenvironmental Engineering*, vol. 127, no. 1, pp. 67–75, 2001.
- [11] M. A. Malusis, S. Yeom, and J. C. Evans, "Hydraulic conductivity of model soil-bentonite backfills subjected to wet-dry cycling," *Canadian Geotechnical Journal*, vol. 48, no. 8, pp. 1198–1211, 2011.
- [12] Y. Wan, Q. Xue, and L. Liu, "Study on the permeability evolution law and the micro-mechanism of CCL in a landfill final cover under the dry-wet cycle," *Bulletin of Engineering Geology and the Environment*, vol. 73, no. 4, pp. 1089–1103, 2014.
- [13] Y.-X. Shen, W.-W. Chen, J. Kuang, and W.-F. Du, "Effect of salts on earthen materials deterioration after humidity cycling," *Journal of Central South University*, vol. 24, no. 4, pp. 796–806, 2017.
- [14] T. D. Wen, L. T. Shao, and X. X. Guo, "Effect of hysteresis on hydraulic properties of soils under multiple drying and wetting cycles," *European Journal of Environmental and Civil Engineering*, vol. 13, 2019.
- [15] M. H. Rayhani, E. K. Yanful, and A. Fakher, "Desiccation-induced cracking and its effect on the hydraulic conductivity of clayey soils from Iran," *Canadian Geotechnical Journal*, vol. 44, no. 3, pp. 276–283, 2007.
- [16] M. H. Rayhani, E. K. Yanful, and A. Fakher, "Physical modeling of desiccation cracking in plastic soils," *Engineering Geology*, vol. 97, no. 1-2, pp. 25–31, 2008.
- [17] H. Lu, J. Li, W. Wang, and C. Wang, "Cracking and water seepage of Xiashu loess used as landfill cover under wetting-drying cycles," *Environmental Earth Sciences*, vol. 74, no. 11, pp. 7441–7450, 2015.
- [18] Y. Wan, Q. Xue, L. Liu, and S. Y. Wang, "Crack characteristic and permeability change of compacted clay liners with different liquid limits under dry-wet cycles," *Advances in Civil Engineering*, vol. 2018, Article ID 5796086, 2018.
- [19] P. Sun, J. Peng, L. Chen, Q. Lu, and O. Igwe, "An experimental study of the mechanical characteristics of fractured loess in western China," *Bulletin of Engineering Geology and the Environment*, vol. 75, no. 4, pp. 1639–1647, 2015.
- [20] W. Han, G. Zhou, D. Gao et al., "Experimental analysis of the pore structure and fractal characteristics of different metamorphic coal based on mercury intrusion-nitrogen adsorption porosimetry," *Powder Technology*, vol. 362, pp. 386–398, 2020.
- [21] W. B. Han, G. Zhou, Q. T. Zhang, H. W. Pan, and D. Liu, "Experimental study on modification of physicochemical characteristics of acidified coal by surfactants and ionic liquids," *Fuel*, vol. 266, Article ID 116966, 2020.
- [22] W. B. Han, G. Zhou, M. Y. Xing et al., "Experimental investigation on physicochemical characteristics of coal treated with synthetic sodium salicylate-imidazole ionic liquids," *Journal of Molecular Liquids*, vol. 2020, Article ID 114822, 2020.
- [23] C. Tang, B. Shi, C. Liu, L. Zhao, and B. Wang, "Influencing factors of geometrical structure of surface shrinkage cracks in clayey soils," *Engineering Geology*, vol. 101, no. 3-4, pp. 204–217, 2008.
- [24] L. F. Pires, O. O. S. Bacchi, and K. Reichardt, "Gamma ray computed tomography to evaluate wetting/drying soil structure changes," *Nuclear Instruments and Methods in Physics Research Section B: Beam Interactions with Materials and Atoms*, vol. 229, no. 3-4, pp. 443–456, 2005.
- [25] L. Pires, O. Bacchi, and K. Reichardt, "Assessment of soil structure repair due to wetting and drying cycles through 2D tomographic image analysis," *Soil and Tillage Research*, vol. 94, no. 2, pp. 537–545, 2007.
- [26] C. Kawaragi, T. Yoneda, T. Sato, and K. Kaneko, "Micro-structure of saturated bentonites characterized by X-ray CT

- observations,” *Engineering Geology*, vol. 106, no. 1-2, pp. 51-57, 2009.
- [27] M. Julina and T. Thyagaraj, “Combined effects of wet-dry cycles and interacting fluid on desiccation cracks and hydraulic conductivity of compacted clay,” *Engineering Geology*, vol. 267, Article ID 105505, 2020.
- [28] L. F. Luo, H. Lin, and P. Halleck, “Quantifying soil structure and preferential flow in intact soil using X-ray computed tomography,” *Soil Science Society of America Journal*, vol. 72, no. 4, 2008.
- [29] Y. Li, S. He, X. Deng, and Y. Xu, “Characterization of macropore structure of Malan loess in NW China based on 3D pipe models constructed by using computed tomography technology,” *Journal of Asian Earth Sciences*, vol. 154, pp. 271-279, 2018.
- [30] S. Peth, R. Horn, F. Beckmann, T. Donath, J. Fischer, and A. J. M. Smucker, “Three-dimensional quantification of intra-aggregate pore-space features using synchrotron-radiation-based microtomography,” *Soil Science Society of America Journal*, vol. 72, no. 4, pp. 897-907, 2008.
- [31] L. Qiu, G. Zhou, W. Z. Zhang, and W. B. Han, “Simulations on the micro-seepage rules of gas and water based on micro-CT/CFD and the related contrastive analysis,” *Arabian Journal of Geosciences*, vol. 12, no. 549, 2019.
- [32] J. Xu, Y. F. Li, C. Ren, S. H. Wang, S. K. Vanapalli, and G. X. Chen, “Influence of freeze-thaw cycles on micro-structure and hydraulic conductivity of saline intact loess,” *Cold Regions Science and Technology*, vol. 181, Article ID 103183, 2020.
- [33] K. Gu, B. Shi, C. Liu, H. Jiang, T. Li, and J. Wu, “Investigation of land subsidence with the combination of distributed fiber optic sensing techniques and microstructure analysis of soils,” *Engineering Geology*, vol. 240, pp. 34-47, 2018.
- [34] C. Liu, B. Shi, J. Zhou, and C. Tang, “Quantification and characterization of microporosity by image processing, geometric measurement and statistical methods: application on SEM images of clay materials,” *Applied Clay Science*, vol. 54, no. 1, pp. 97-106, 2011.
- [35] C. Liu, C.-S. Tang, B. Shi, and W.-B. Suo, “Automatic quantification of crack patterns by image processing,” *Computers & Geosciences*, vol. 57, pp. 77-80, 2013.
- [36] R. P. Chapuis, “Predicting the saturated hydraulic conductivity of sand and gravel using effective diameter and void ratio,” *Canadian Geotechnical Journal*, vol. 41, no. 5, pp. 787-795, 2004.
- [37] M. Mbonimpa, M. Aubertin, R. P. Chapuis, and B. Bussière, “Practical pedotransfer functions for estimating the saturated hydraulic conductivity,” *Geotechnical and Geological Engineering*, vol. 20, no. 3, pp. 235-259, 2002.
- [38] D. W. Taylor, *Fundamentals of Soil Mechanics*, Wiley, New York, NY, USA, 1948.
- [39] G. Mesri and F. Tavenas, “Discussion of “permeability and consolidation of normally consolidated soils” by A. Mahinda samarasinghe, Yang H. Huang, and Vincent P. Drnevich (June, 1982),” *Journal of Geotechnical Engineering*, vol. 109, no. 6, pp. 873-878, 1983.
- [40] A. M. Samarasinghe, Y. H. Huang, and V. P. Drnevich, “Permeability and consolidation of normally consolidated soils,” *Journal of the Geotechnical Engineering Division*, vol. 108, no. 6, pp. 835-850, 1982.
- [41] W. Z. Liu, M. L. Shi, and L. C. Miao, “Experimental study of permeability coefficient of natural saturated clay and its prediction model,” *Rock and Soil Mechanics*, vol. 34, no. 9, pp. 2501-2507+2514, 2013, in Chinese.